




## Article

# Synthesis of BiOCl Colloidal Particles by Laser Ablation of Solids in Liquids

Abril Vázquez Francisco <sup>1</sup>, Armando Pérez-Centeno <sup>2</sup>, Laura P. Rivera <sup>2</sup> and José G. Quiñones-Galván <sup>2,\*</sup>

<sup>1</sup> Departamento de Ingeniería de Proyectos, CUCEI Universidad de Guadalajara, Blvd. Marcelino García Barragán, Guadalajara 44430, Jalisco, Mexico; abril.vazquez4166@alumnos.udg.mx

<sup>2</sup> Departamento de Física, CUCEI Universidad de Guadalajara, Blvd. Marcelino García Barragán, Guadalajara 44430, Jalisco, Mexico; armando.centeno@academicos.udg.mx (A.P.-C.); laura.rivera@academicos.udg.mx (L.P.R.)

\* Correspondence: jose.quinones@academicos.udg.mx

**Abstract:** Colloidal bismuth nanoparticles (NPs) were synthesized in sodium chloride (NaCl) solutions at different concentrations using the laser ablation of solids in liquids technique. The obtained materials were characterized using various techniques. The morphology, size, and crystalline phases were determined through scanning electron microscopy (SEM), transmission electron microscopy (TEM), X-ray photoelectron spectroscopy (XPS), Raman spectroscopy, and Fourier-transform infrared spectroscopy (FTIR). The optical properties were studied using UV–visible spectroscopy, employing the Tauc method to determine the band gap of the particles. Two types of materials were identified depending on the NaCl concentration: spherical nanoparticles of  $\alpha$ -Bi<sub>2</sub>O<sub>3</sub> and the coexistence of  $\alpha$ -Bi<sub>2</sub>O<sub>3</sub> and BiOCl particles with irregular morphology. NaCl concentrations higher than 11.6% enable the coexistence of  $\alpha$ -Bi<sub>2</sub>O<sub>3</sub> and BiOCl. The photocatalytic response of the colloids was evaluated by the degrading rhodamine B under visible light irradiation. The sample synthesized at a NaCl concentration of 31.6% showed the best photocatalytic activity.

**Keywords:** BiOCl; laser ablation; colloidal particles



**Citation:** Vázquez Francisco, A.; Pérez-Centeno, A.; Rivera, L.P.; Quiñones-Galván, J.G. Synthesis of BiOCl Colloidal Particles by Laser Ablation of Solids in Liquids. *Surfaces* **2024**, *7*, 864–878. <https://doi.org/10.3390/surfaces7040057>

Academic Editor: Kurt W. Kolasinski

Received: 8 August 2024

Revised: 4 October 2024

Accepted: 10 October 2024

Published: 15 October 2024



**Copyright:** © 2024 by the authors. Licensee MDPI, Basel, Switzerland. This article is an open access article distributed under the terms and conditions of the Creative Commons Attribution (CC BY) license (<https://creativecommons.org/licenses/by/4.0/>).

## 1. Introduction

Bismuth oxide (Bi<sub>2</sub>O<sub>3</sub>) is a semiconductor material that presents polymorphism in six different crystalline phases:  $\alpha$  and  $\delta$  (stable phases) and  $\beta$ ,  $\gamma$ ,  $\epsilon$ , and  $\omega$  (metastable phases at high temperatures) [1,2]. Due to its electronic properties and low toxicity, Bi<sub>2</sub>O<sub>3</sub> has been used in multiple applications, such as the fabrication of gas sensors, electrochemical sensors, antimicrobial agents, and photocatalysts [1,3]. On the other hand, bismuth oxychloride (BiOCl) belongs to the compounds known as bismuth oxyhalides (BiOX), which are semiconducting materials with a lamellar structure. The Cl-Bi-O-Bi-Cl layered structure, along with its low toxicity at small concentrations (less than 0.5  $\mu\text{g}/\text{mL}$ ) [4] and its band gap, which ranges between 3.2 eV and 3.5 eV, make BiOCl suitable for use as a photocatalyst when exposed to UV light [5].

In recent decades, nanomaterials based on Bi<sub>2</sub>O<sub>3</sub> and BiOCl have attracted significant interest from the scientific community due to their application in the photodegradation of organic pollutants. Key areas of research include synthesis methods, doping, and the morphology control of Bi<sub>2</sub>O<sub>3</sub> and BiOCl nanostructures to enhance their photocatalytic activity. Ghadi et al. reported that the  $\alpha$  and  $\beta$  phases of Bi<sub>2</sub>O<sub>3</sub> can degrade indigo carmine (IC) and rhodamine B (RhB) under UV and visible light irradiation, with higher efficiency under UV irradiation [6]. Furthermore, they demonstrated that an  $\alpha/\beta$ -Bi<sub>2</sub>O<sub>3</sub> heterojunction obtained through a solid state reaction–annealing route achieves a higher degradation rate of IC and RhB compared to the individual  $\alpha$  and  $\beta$  phases of Bi<sub>2</sub>O<sub>3</sub>. Li et al. reported the synthesis of BiOCl nanolayers using a solvothermal method with bismuth nitrate pentahydrate (Bi(NO<sub>3</sub>)<sub>3</sub>•5H<sub>2</sub>O), sodium chloride (NaCl), and ethylene

glycol (C<sub>2</sub>H<sub>6</sub>O<sub>2</sub>) as precursors. These nanostructures were successfully used to degrade RhB under visible light irradiation, achieving a 97% degradation of the contaminant within 20 min of exposure to visible light [7].

Bismuth compounds can be synthesized through various methods, with the laser ablation of solids in liquids (LASL) technique being one of the most commonly used due to its versatility. LASL enables the synthesis of nanoparticles (NPs) by impinging high-power laser pulses onto a target submerged in a liquid solution. In recent years, the LASL technique has been employed to obtain a wide range of nanomaterials with minimal modifications to the experimental process. Lin et al. reported the synthesis of spherical and quasi-spherical  $\alpha$ -Bi<sub>2</sub>O<sub>3</sub> NPs via laser ablation in ethanol [8]. These NPs demonstrated photocatalytic activity in the degradation of IC when irradiated by a commercial 365 nm LED.

On the other hand, BiOCl NPs are mostly synthesized through the hydrothermal method, using water, hydrochloric acid, sodium chloride, or bismuth chloride (BiCl<sub>3</sub>) as precursors [7,9,10]. The LASL technique provides an alternative synthesis route for this type of NPs, reducing both the synthesis time and the amount of chemical reagents used, while also allowing control over the NPs' morphology by adjusting the laser parameters [11]. In the literature, the use of HCl, a common precursor of the hydrothermal method, has been reported in the synthesis of spherical BiOCl NPs via LASL [12–14]. These NPs exhibit different properties compared to those synthesized by the hydrothermal method, such as improved morphology and a reduction in their band gap value, which is a key parameter related to the photocatalytic activity of the material. Additionally, Wei et al. reported that BiOCl nanosheets exhibit photocatalytic activity on RhB degradation under visible light irradiation. This photocatalytic activity was further enhanced by decorating the BiOCl nanosheets with gold nanoparticles [14].

It is known that NaCl, a common precursor in the hydrothermal method, has been used as a stabilizing agent in the synthesis of metal nanoparticles via the LASL technique [15,16]. However, to date, the use of NaCl solutions for the synthesis of bismuth nanoparticles through LASL remains unexplored. Consequently, the feasibility of employing NaCl to synthesize BiOCl NPs through LASL, as well as the impact of this precursor on the band gap value and photocatalytic activity of Bi<sub>2</sub>O<sub>3</sub> and BiOCl NPs, has not yet been fully understood. The present study focuses on the synthesis of bismuth compounds nanoparticles using the LASL technique, employing a bismuth target submerged in solutions with different concentrations of NaCl. The differences in the NaCl concentration allowed for the evaluation of how this precursor influences the transformation of Bi nanoparticles into Bi<sub>2</sub>O<sub>3</sub> and BiOCl NPs, which were subsequently tested for their photocatalytic activity in the degradation of rhodamine B.

## 2. Materials and Methods

### Synthesis of bismuth NPs

Colloidal bismuth nanoparticles were synthesized using the LASL technique. The experimental setup is illustrated in Figure 1a. For this experiment, a Nd:YAG laser (Q-Smart 850, Quantel, Newbury, UK) with a wavelength of 1064 nm, pulse duration of 6 ns, and operating frequency of 10 Hz was used. A bismuth target (3 cm in diameter, 0.5 cm thick, 99.9% purity) was placed into a glass container filled with 10 mL of NaCl solutions at various concentrations (0%, 3%, 11.6%, 31.6%, by weight). The laser was directed at the surface of the bismuth target using a series of mirrors. The target was kept fixed and ablated using a fluence of 0.51 J/cm<sup>2</sup>, achieved with an energy of 324 mJ per pulse and a spot size of 0.64 cm<sup>2</sup>. The spot size was determined by measuring the ablation mark (9 mm diameter) on the target after the experimental process. After 300 laser pulses were applied to the bismuth target, a dark brown colloidal nanoparticle suspension was produced and collected in glass containers for further characterization (Figure 1b).

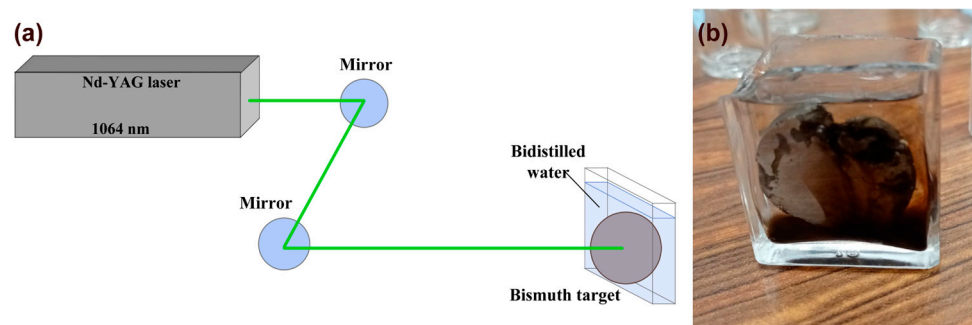


**Figure 1.** (a) Schematic illustration of the synthesis process and (b) nanoparticle colloidal solution obtained.

The characterization of the obtained colloids was performed without prior washing, as the small amount of ablated material made its recovery difficult after washing processes and led to a significant loss of the material of interest. The colloidal nanoparticle suspensions were stored in glass containers until the time of characterization.

#### Characterization of synthesized materials

The morphology of the synthesized materials was analyzed by scanning electron microscopy (SEM) using a TESCAN MIRA 3 microscope (TESCAN, Seoul, Republic of Korea) operating at 20 KV. A drop of the material was deposited onto  $10 \times 8 \text{ mm}^2$  silicon substrates, and the samples were dried at room temperature for 24 h. Transmission electron microscopy (TEM) was also employed for morphological characterization, using a JEOL JEM 1010 instrument (JEOL, Tokyo, Japan) at 90 kV to examine the size of the synthesized NPs. A drop of the sample was deposited on a 3 mm diameter grid, and the liquid medium was evaporated at room temperature.

The optical properties of the synthesized materials were studied using UV–visible spectroscopy. A Thermo Fisher Scientific Genesys 10 UV–visible spectrophotometer (Thermo Fisher Scientific, Waltham, MA, USA) was used to obtain spectra in the 200 to 500 nm range for each synthesized material. UV–visible spectra were obtained on the day of ablation, as well as 3 and 28 days afterward. The UV–visible data were used to plot Tauc graphs to estimate the optical band gap of the materials.

The chemical state of the samples was analyzed using X-ray photoelectron spectroscopy (XPS) to determine the binding energies of Bi, Cl, and O in the materials. A SPECS spectrometer (SPECS, Berlin, Germany) equipped with a PHOIBOS 150 and an Al  $K_{\alpha}$  X-ray monochromator was used to carry out scans of the samples, which were deposited on silicon substrates. XPS spectra were calibrated using the C 1s peak.

The crystalline phases and chemical species of the synthesized materials were characterized by Raman spectroscopy, obtaining spectra in the range of  $52$  to  $3374 \text{ cm}^{-1}$  with a 785 nm excitation source, using a Thermo Scientific equipment model, DRX2 Smart. For this analysis, a drop of each material was deposited on silicon substrates, and the liquid medium was evaporated at room temperature. The functional groups present in the synthesized materials were characterized using infrared spectroscopy with a Nicolet iS50 FT-IR spectrometer from Thermo Scientific. A drop of each sample was deposited on silicon substrates, and the liquid medium was evaporated at room temperature.

#### Photocatalytic activity

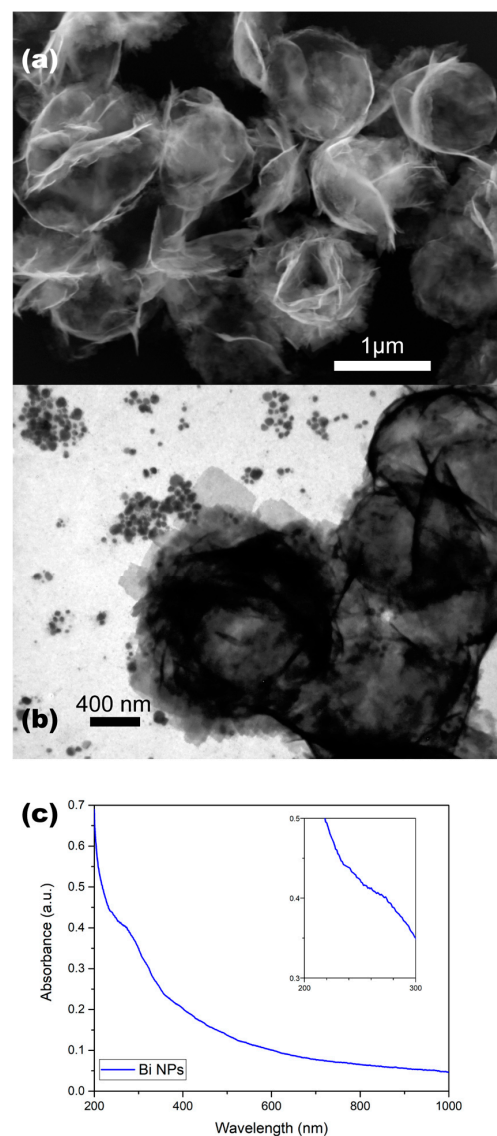
The materials synthesized in the presence of NaCl were tested as photocatalysts. The photocatalytic activity of these materials was evaluated based on the degradation of rhodamine B (10 mg/L). For sample preparation, 3 mL of synthesized material and 1 mL of rhodamine B were placed inside test tubes. Prior to conducting the photocatalysis test, the solutions were stirred in the dark for 48 h to achieve adsorption–desorption equilibrium between the rhodamine B and the synthesized materials. The test tubes were then exposed to visible light from a fluorescent lamp positioned 10 cm away. After irradiation, the

samples were analyzed using UV–visible spectroscopy at intervals of 30, 60, 90, 180, and 720 min.

### 3. Results and Discussion

#### Bi NPs in distilled water

Colloidal solutions of bismuth nanoparticles synthesized in water were analyzed by UV–visible, SEM, and TEM techniques, at 7, 13, and 15 days after synthesis, respectively. A SEM micrograph of the synthesized NPs is shown in Figure 2a. In this image, quasi-spherical morphologies with diameters ranging from 0.8 to 1.2  $\mu\text{m}$  can be seen, composed of planes oriented in multiple directions. Figure 2b corresponds to an image of the same sample, acquired by TEM at 50,000 magnifications. The same quasi-spherical structures composed of nanosheets oriented in multiple directions are visible, along with structures smaller than 100 nm in diameter, distributed around the larger morphologies. In both images, the larger-sized structures correspond to morphologies called nanoflowers, which can be associated with oxidized bismuth nanoparticles forming bismuth carbonate ( $(\text{BiO})_2\text{CO}_3$ ). Layered structures similar to the ones observed in Figure 2 are typical for bismuth carbonates synthesized by laser ablation of Bi in water [17].



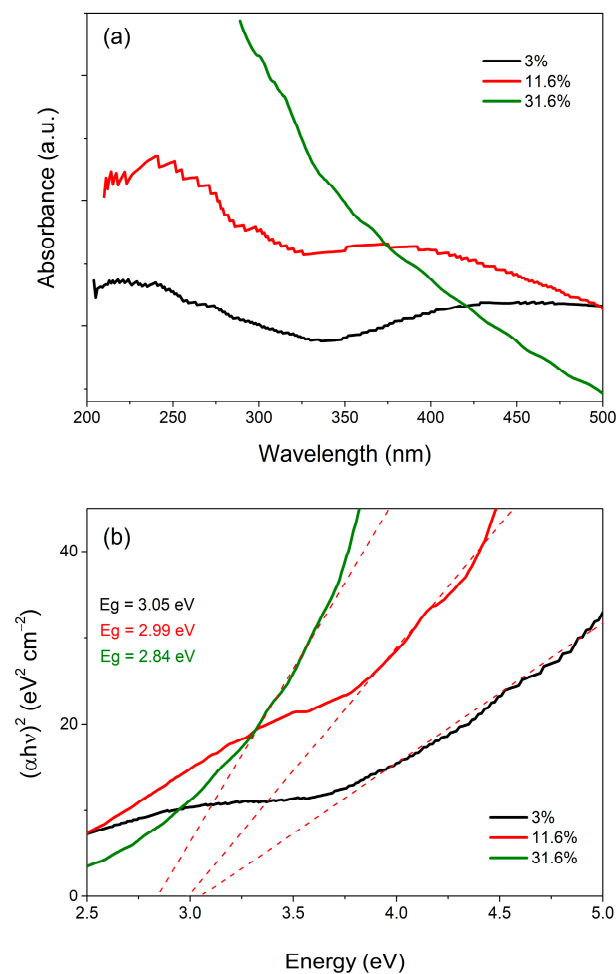
**Figure 2.** Bismuth nanoparticles after the synthesis: (a) SEM micrograph, (b) TEM micrograph, and (c) UV–vis spectrum.



Figure 2c shows the optical absorbance of bismuth NPs. The inset in Figure 2c provides a close-up view of the 200–300 nm range of the plot. In this inset, bands can be observed at 237 and 285 nm, which correspond to the presence of Bi and  $(\text{BiO})_2\text{CO}_3$  NPs, respectively [12,17].

#### Oxidation of Bi NPs in the presence of NaCl

The oxidation of bismuth nanoparticles in the presence of NaCl was monitored using UV–visible spectroscopy. The results are shown in Figure 3a. At a 3% NaCl concentration, a band at 239 nm and a shoulder at 271 nm were observed, corresponding to the presence of Bi NPs and  $\text{Bi}_2\text{O}_3$ , respectively [12]. As the NaCl concentration increased, bands associated with  $\text{BiOCl}$  emerged, while bands associated with Bi NPs disappeared [12]. Figure 3b shows the Tauc plot of the synthesized materials. The Tauc plots show band gap values of 3.05 eV, 2.99 eV, and 2.84 eV for materials synthesized with 3%, 11.6%, and 31.6% NaCl, respectively. These values are associated with the presence of  $\text{Bi}_2\text{O}_3$  and are lower than the band gap values for  $\text{BiOCl}$  [14,18]. The Tauc plots indicate that the optical transitions of the synthesized materials are dominated by the direct transition of  $\text{Bi}_2\text{O}_3$ , making it difficult to observe the indirect transition corresponding to  $\text{BiOCl}$ . Contrary to expectations, no proportional coefficient was found between NaCl concentration and changes in the band gap value. This may be due to differences in the composition and morphology of the synthesized materials that could modify their optical band gap.



**Figure 3.** UV–vis spectra (a) and Tauc plots (b) of the samples synthesized at different concentrations of NaCl.

The SEM and TEM micrographs of the four samples were obtained 28 days after the synthesis process. The SEM and TEM images of the samples synthesized with 3% NaCl are

shown in Figure 4. The SEM micrograph, presented in Figure 4a, shows that the morphology of the synthesized material consists of quasi-spherical structures with a diameter smaller than 100 nm, which are grouped in clusters. The TEM image (Figure 4b) shows that the smallest particles in the sample have diameters ranging from 10 to 50 nm. These nanoparticles are grouped to form quasi-spherical structures and clusters, as observed in the lower-left corner of the micrograph. Spectroscopic analysis identifies the morphologies observed in Figure 3 as  $\alpha$ - $\text{Bi}_2\text{O}_3$  nanoparticles. These nanoparticles do not have morphological similarities with the  $(\text{BiO})_2\text{CO}_3$  nanoflowers present in the sample synthesized without NaCl, suggesting that NaCl influences the size and morphology of the NPs.

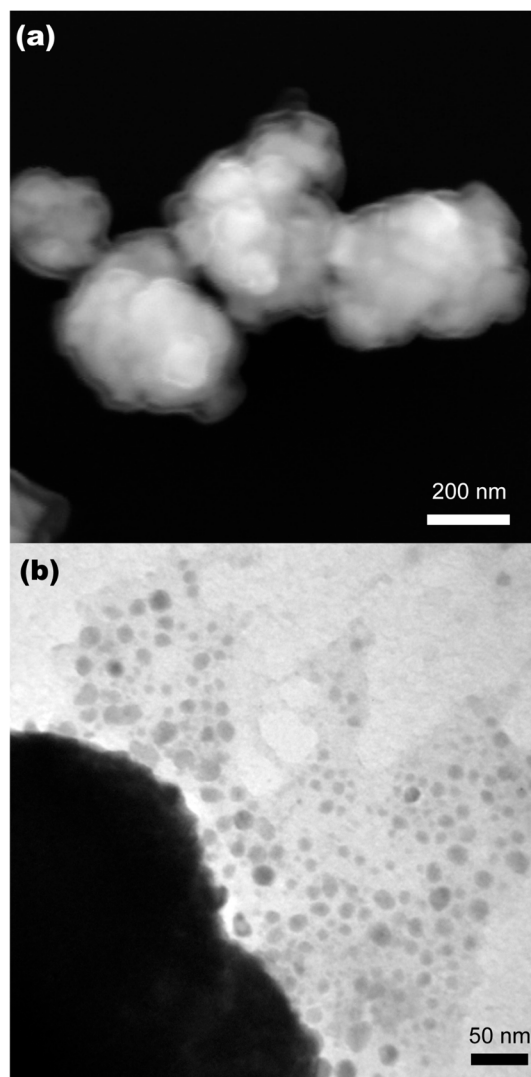


**Figure 4.** (a) SEM and (b) TEM micrographs of bismuth NPs in 3% NaCl solution.

The morphology of the sample synthesized with 11.6% NaCl is shown in Figure 5. This sample consists of clusters of quasi-spherical particles, named nano-cottons. The diameter of the nano-cottons ranges from 200 to 250 nm, as observed in the SEM micrograph (Figure 5a). In contrast, the TEM micrograph (Figure 5b) reveals smaller particles, with diameters less than 50 nm. Spectroscopic analysis determined that this sample consists of both  $\alpha$ - $\text{Bi}_2\text{O}_3$  and  $\text{BiOCl}$ . The structures observed in Figure 5 are identified as  $\alpha$ - $\text{Bi}_2\text{O}_3$  nano-cottons, given the higher abundance of  $\alpha$ - $\text{Bi}_2\text{O}_3$ , compared to  $\text{BiOCl}$  in this sample, as well as the similarity of the nano-cottons to the NPs clusters in the sample synthesized with 3% NaCl.

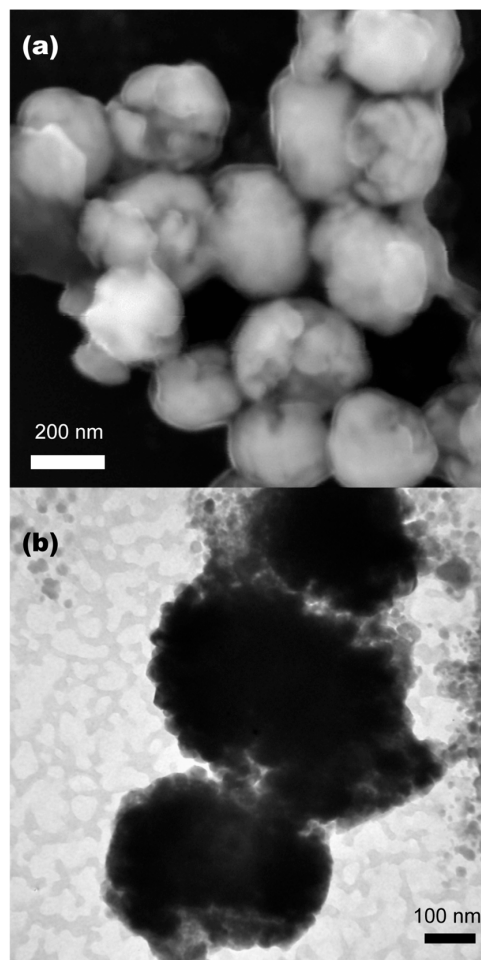


**Figure 5.** (a) SEM and (b) TEM micrographs of bismuth NPs in 11.6% NaCl solution.

The sample synthesized with 31.6% NaCl presents crystalline clusters of sodium chloride, as shown in Figure 6a, which do not allow the identification of smaller structures in the observed area of the sample. The TEM micrograph of the sample (Figure 6b) shows a structure with irregular morphology and dimensions of  $150 \times 300 \text{ nm}^2$ . This sample does not exhibit morphological similarities with the nanostructures observed in the samples synthesized with 3% and 11.6% NaCl, suggesting that these irregular structures could correspond to BiOCl.

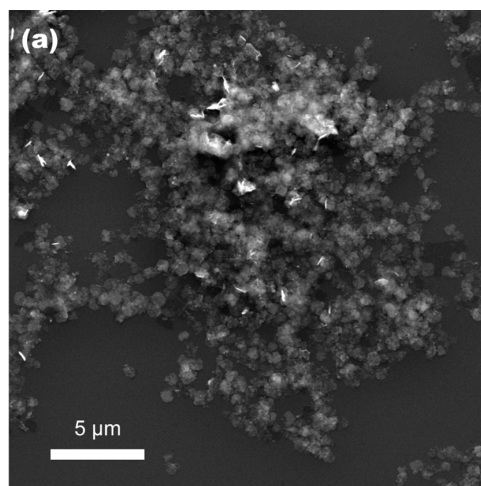


**Figure 6.** Cont.

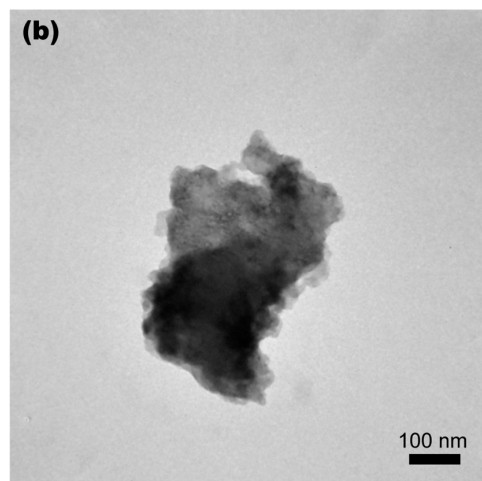


**Figure 6.** (a) SEM and (b) TEM micrographs of bismuth NPs in 31.6% NaCl solution.

Figure 7 shows the X-ray emitted photoelectron spectroscopy (XPS) survey spectra of the four samples. In these spectra, signals corresponding to Bi 4f, Cl 2p, and O 1s can be identified, in addition to Si 2p and Na 1s signals from the substrate and precursor.

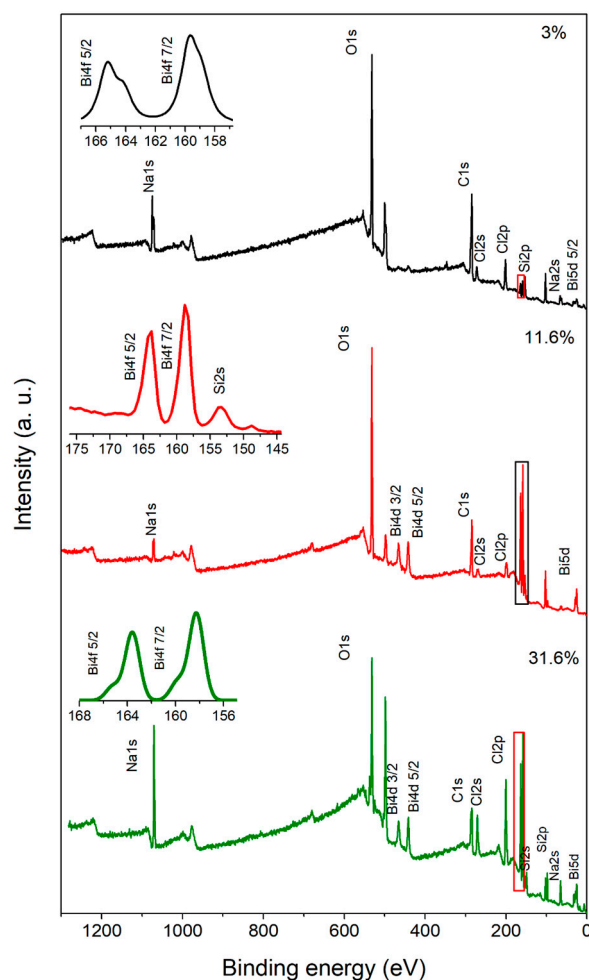


**Figure 7.** Survey XPS spectra of the samples synthesized with 3%, 11.6%, and 31.6% NaCl.

The high-resolution spectra for the Bi 4f region are shown in Figure 8. The sample synthesized with 3% NaCl exhibits peaks at binding energies of 159.7 and 165.2 eV, corresponding to the Bi 4f 7/2 and Bi 4f 5/2 levels, respectively. Two additional lower-intensity

peaks are centered at 158.8 and 164.1 eV, indicating the presence of  $\text{Bi}_2\text{O}_3$  [18]. The sample synthesized with 11.6% NaCl shows two peaks associated with the presence of  $\text{Bi}_2\text{O}_3$  at binding energies of 158.8 and 164.1 eV. Lower-intensity peaks at 160 and 165.25 eV correspond to  $\text{BiOCl}$  [10,11]. The spectra of the sample synthesized with 31.6% NaCl shows four peaks. The peaks at binding energies of 158.3 and 163.6 eV are associated with  $\text{Bi}_2\text{O}_3$ , while lower-intensity peaks at 159.8 and 165.2 eV correspond to  $\text{BiOCl}$ .

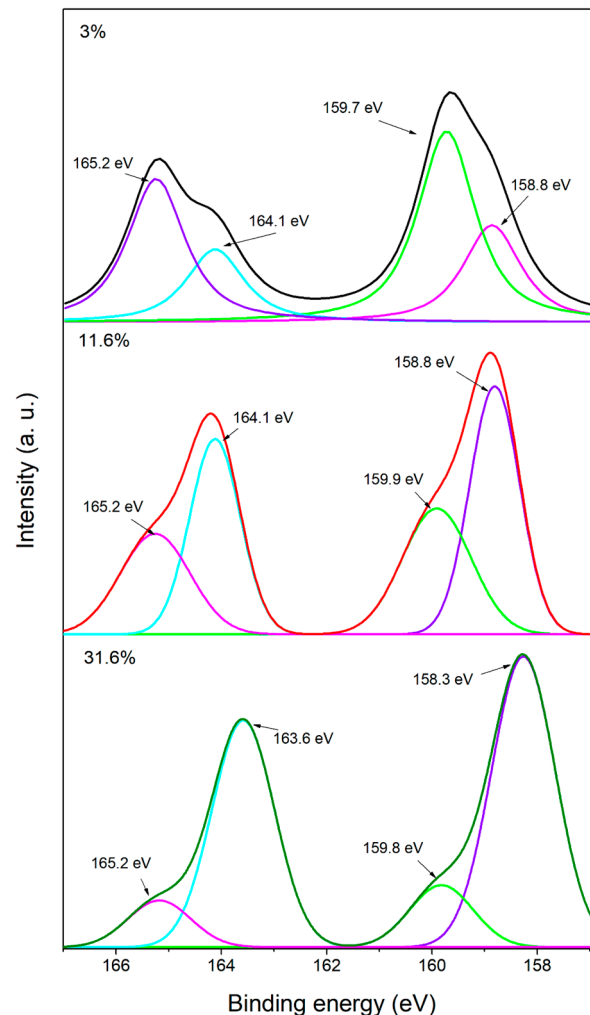


**Figure 8.** High resolution XPS spectra of Bi 4f.

Figure 9 shows the high resolution XPS spectra in the Cl 2p region. The sample synthesized with 3% NaCl exhibits peaks at 202.3 and 203.7 eV, corresponding to the Cl 2p 3/2 and Cl 2p 1/2 levels, respectively. None of these peaks are associated with Bi-Cl bonds. The sample synthesized with 11.6% NaCl shows four peaks in its high-resolution spectra, with binding energies of 199.2 and 200.8 eV, characteristic of the  $\text{Cl}^-$  ion in  $\text{BiOCl}$  molecules [19]. In the sample synthesized with 31.6% NaCl, the peaks at binding energies of 198.6 and 200.2 eV correspond to  $\text{BiOCl}$ .

The O 1s spectra are shown in Figure 10. The sample synthesized with 3% NaCl shows two peaks at binding energies of 530.5 and 532.1 eV. The peak at 530.5 eV corresponds to the Bi-O interaction present in the sample [20], while the peak at 532.1 eV is attributed to the presence of  $\text{SiO}_2$ , resulting from the interaction between the substrate and the environment [21]. The sample synthesized with 11.6% NaCl shows three peaks at 530.6, 532.2, and 533.5 eV. The peaks at 530.6 and 532.2 eV correspond to the Bi-O interaction and the  $\text{SiO}_2$  presence, respectively. The peak at 533.5 eV is associated with the presence of -OH radicals in the material [22]. The high-resolution spectra of the sample synthesized



with 31.6% NaCl shows three peaks at 529.8, 531.4, and 532.5 eV, corresponding to the Bi-O interaction, as well as the presence of SiO<sub>2</sub> and -OH radicals in the sample, respectively.

As the NaCl concentration increases, the intensity difference between the peaks associated with Bi<sub>2</sub>O<sub>3</sub> and the additional peaks at the Bi 4f level increases, indicating the influence of NaCl on compound formation. In the case of the sample synthesized with 3% NaCl, peaks with binding energies potentially related to the presence of BiOCl are observed at the Bi 4f and O 1s levels; however, the Cl 2p level does not show signals corresponding to Bi-Cl bonds.

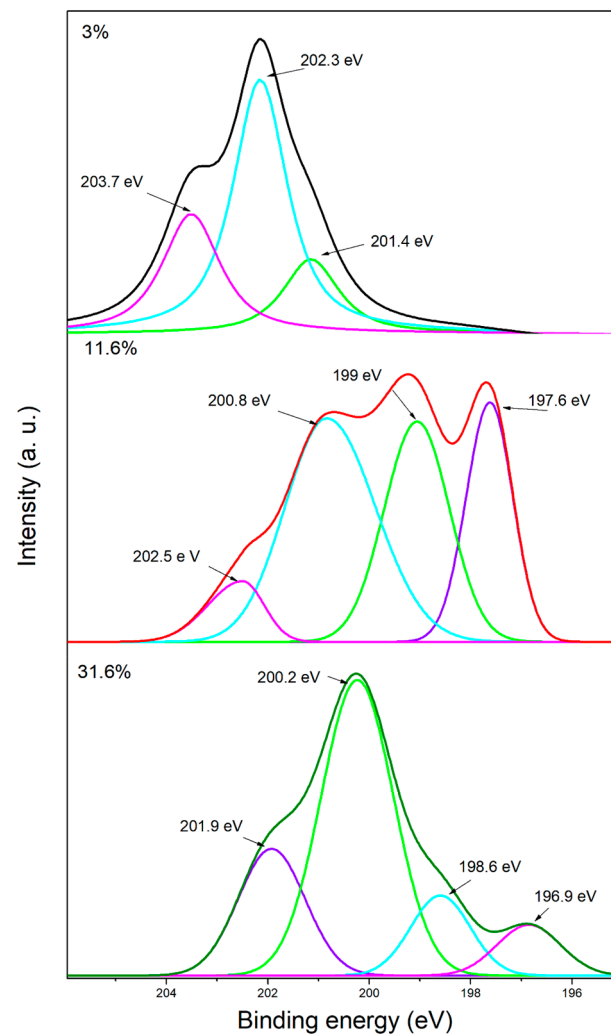


**Figure 9.** High resolution XPS spectra of Cl 2p.

The results of Raman spectroscopy are shown in Figure 11. At a 3% NaCl concentration, small bands are observed at 73, 93, 106, 125, and 156 cm<sup>-1</sup>, which are associated with the presence of  $\alpha$ -Bi<sub>2</sub>O<sub>3</sub> [11,23]. As the NaCl concentration increases to 11.6%, the Raman spectrum changes: the band at 156 cm<sup>-1</sup> disappears, and a new band appears at 138 cm<sup>-1</sup>, corresponding to the presence of BiOCl [12,24]. Unlike the UV-visible analysis, none of the Raman spectra show characteristic bands of Bi NPs, which may be attributed to the time elapsed between synthesis and the Raman spectroscopy analysis, allowing the complete oxidation of the bismuth. It is also observed that as the NaCl concentration increases, the presence of bands associated with BiOCl also increases.

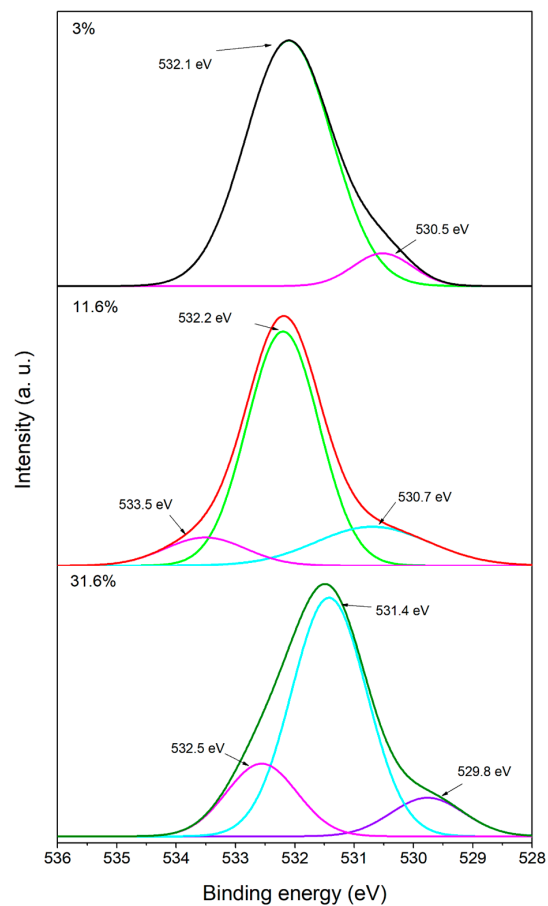


Figure 10. High resolution XPS spectra of O 1s.

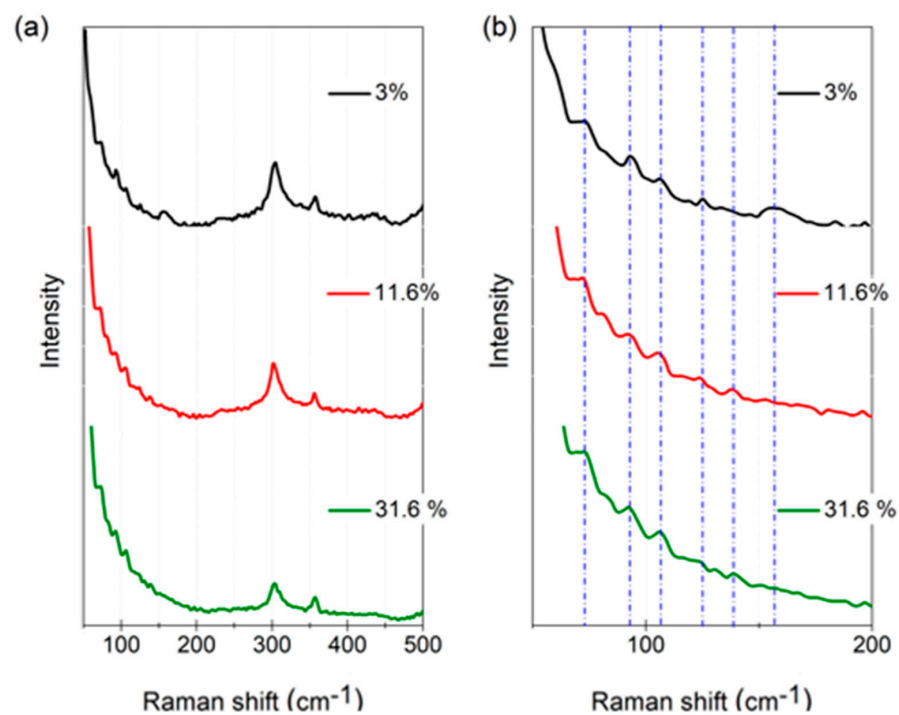
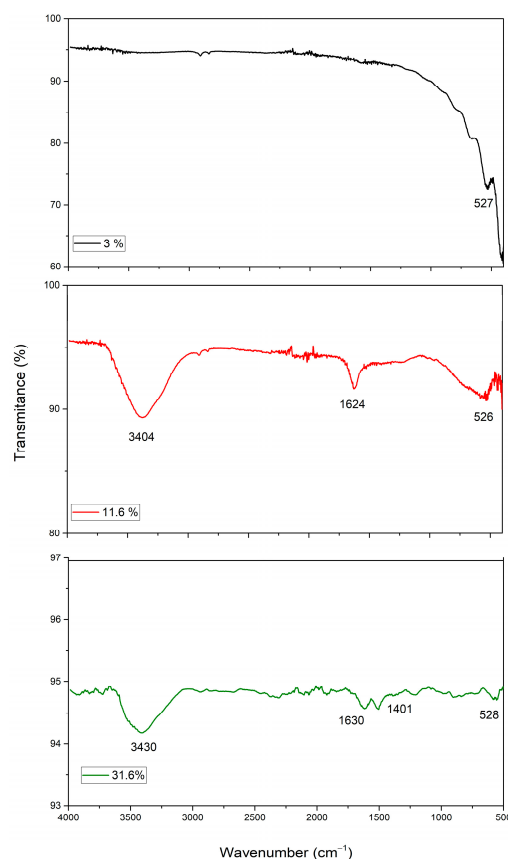


Figure 11. Raman spectra of the samples synthesized at different NaCl concentrations showing the following: (a) the full Raman spectrum, (b) magnification of the Raman bands for  $\text{Bi}_2\text{O}_3$ , and  $\text{BiOCl}$ .

Although additional techniques, such as XRD and EDS, could provide complementary insights into the crystalline phases and composition of the synthesized materials, the limited sample quantity made proper preparation for XRD characterization challenging. Therefore, XPS and Raman spectroscopy were selected as the primary characterization methods, as they are sufficiently sensitive to identify the sample composition and the vibrational modes corresponding to  $\text{Bi}_2\text{O}_3$  and  $\text{BiOCl}$ . XPS measurements provided reliable data on the oxidation states of the elements, while the sensitivity of Raman spectroscopy to the vibrational modes of  $\text{BiOCl}$  effectively confirmed its presence. While these techniques have been adequate for the objectives of this study, we acknowledge that a more comprehensive structural and chemical characterization using XRD and EDS, respectively, could further strengthen the conclusions. These characterizations will be considered in future studies, especially as larger sample quantities become available, and thorough washing is performed to eliminate potential  $\text{NaCl}$  residues.

Figure 12 shows the FT-IR spectra of the synthesized materials. All spectra share a common band, between  $527$  and  $528\text{ cm}^{-1}$ , which is attributed to the vibration of Bi-O bonds [25,26]. The FT-IR spectra of the materials synthesized with 11.6% and 31.6%  $\text{NaCl}$  show bands indicating the presence of O-H and H-O-H bonds, associated with the hydration of the samples at the time of analysis. These bands are observed in the ranges of  $3404$ – $3430\text{ cm}^{-1}$  and  $1624$ – $1630\text{ cm}^{-1}$ , respectively. As the  $\text{NaCl}$  concentration increases to 31.6%, a band at  $1401\text{ cm}^{-1}$ , corresponding to the vibration of Bi-Cl bonds, becomes apparent [27]. The presence of Bi-Cl bonds confirms the formation of  $\text{BiOCl}$  in the oxidized NPs synthesized with 31.6%  $\text{NaCl}$ , consistent with the UV-visible and Raman results. The FT-IR analysis does not confirm the presence of  $\text{BiOCl}$  in the material synthesized with 11.6%  $\text{NaCl}$ , suggesting that the vibrations associated with Bi-Cl bonds in this sample are much weaker compared to those of O-H, H-O-H, and Bi-O bonds, making them undetectable by FT-IR.



**Figure 12.** FT-IR spectra of the samples.

### Photocatalytic activity

The time evolution of the photocatalytic degradation of rhodamine B was analyzed by UV–visible spectroscopy. The absorbance of the samples was measured after 30, 60, 90, 180, and 720 min. After 720 min, the samples synthesized with 3% and 11.6% NaCl have a paler pink tone compared to their original color before irradiation, as shown in Figure 13. In contrast, the sample synthesized with 31.6% NaCl exhibits a pale green tone. Figure 14 shows the percentage of rhodamine B remaining in the samples after each irradiation period. The curve for the sample synthesized with 31.6% NaCl shows the highest degradation of rhodamine B, with a final concentration of 37.81%, in comparison to the 3% NaCl sample, which retained 80.27% of the rhodamine B.

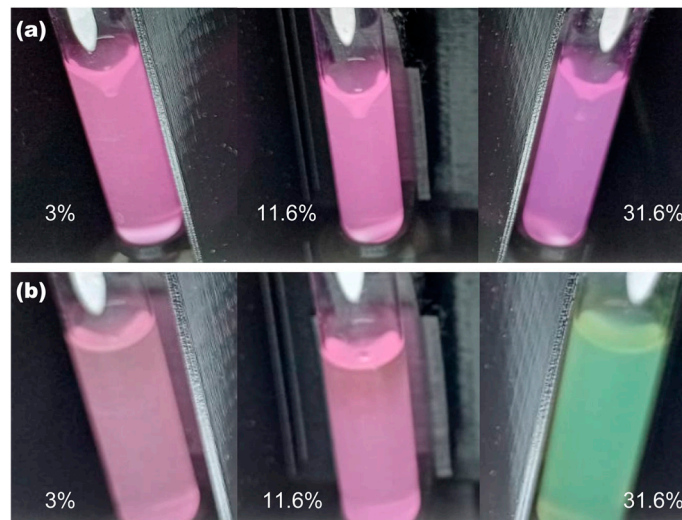


**Figure 13.** Rhodamine B+Bi NPS solutions: (a) before being irradiated with visible light, (b) after 720 min of irradiation.

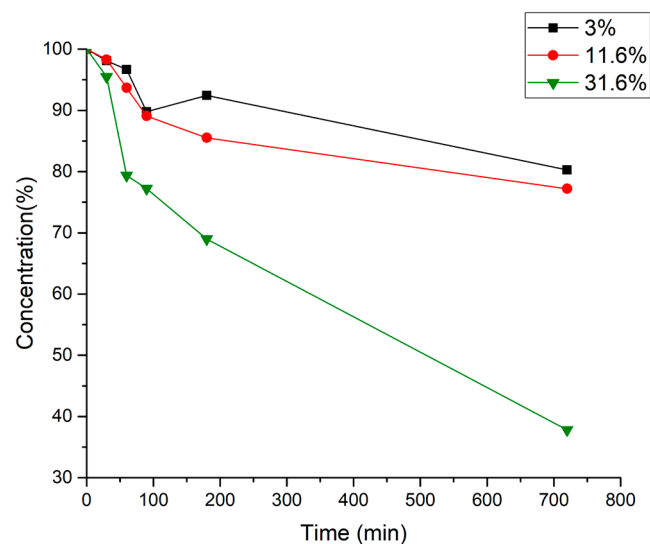


**Figure 14.** Photocatalytic degradation of rhodamine B using bismuth NPs synthesized in 3%, 11.6%, and 31.6% of NaCl, under visible light radiation.

The analysis of the graph in Figure 14 reveals that the percentage of rhodamine B degradation increases with higher NaCl concentrations. However, the degradation percentage does not correlate with the band gap value of the samples. This may be due to the morphology of the synthesized materials, which can be modified by increasing the NaCl concentration, consequently enhancing the photocatalytic activity of the material.

#### 4. Conclusions

The use of NaCl solutions is effective for the synthesis of  $\alpha$ -Bi<sub>2</sub>O<sub>3</sub> and BiOCl by the LASL technique. The XPS characterization demonstrates that NaCl concentrations above 11.6% are effective in producing a colloidal suspension containing both  $\alpha$ -Bi<sub>2</sub>O<sub>3</sub> and BiOCl, while lower concentrations yield only Bi<sub>2</sub>O<sub>3</sub>. TEM and SEM analyses revealed that both  $\alpha$ -Bi<sub>2</sub>O<sub>3</sub> nanoparticles and BiOCl particles were synthesized, with their size and morphology depending on the NaCl concentration. NaCl concentrations of 11.6% or less favor the formation of spherical nanoparticles aggregated in nano-cottons, while higher concentrations, higher than 11.6% NaCl, generate particles with irregular morphology and sizes exceeding 150 × 300 nm<sup>2</sup>. The band gap of the nanoparticles differs from that of the NPs synthesized without NaCl; however, the results indicate that the band gap is not directly dependent on the NaCl concentration. When evaluating the photocatalytic activity, it was found that the percentage of RhB degradation is influenced by the NaCl concentration. NaCl concentrations below 31.6% resulted in photocatalytic activity of less than 20% after 720 min, while the sample synthesized with 31.6% NaCl showed the highest photocatalytic activity, with 62.19% degradation after 720 min.

**Author Contributions:** Conceptualization, J.G.Q.-G. and A.V.F.; methodology, A.V.F. and A.P.-C.; formal analysis, J.G.Q.-G., A.V.F., A.P.-C. and L.P.R.; investigation, A.V.F.; writing—original draft preparation, A.V.F.; writing—review and editing, J.G.Q.-G., A.P.-C. and L.P.R. All authors have read and agreed to the published version of the manuscript.

**Funding:** This research was funded by Universidad de Guadalajara.

**Institutional Review Board Statement:** Not applicable.

**Informed Consent Statement:** Not applicable.

**Data Availability Statement:** Data are available upon request.

**Acknowledgments:** The authors acknowledge Agustín Lara for conducting the Raman measurements at LAFE and Cecilia Sánchez Jiménez for the FT-IR measurements. Jose Antonio Rivera Mayorga is acknowledged for the XPS measurements. The authors acknowledge CONACYT, project grant 270662. Universidad de Guadalajara is acknowledged for financial support.

**Conflicts of Interest:** The authors declare no conflicts of interest. The funders had no role in the design of this study; in the collection, analyses, or interpretation of the data; in the writing of the manuscript; or in the decision to publish the results.

#### References

1. Elizarraras-Peñaloza, A.; Estrada-Flores, M.; Germán, R.S.; Manríquez Ramírez, M.E.; Díaz Barriga-Arceo, L.G.; Santiago-Jacinto, P. Change of phase from  $\alpha$ -Bi<sub>2</sub>O<sub>3</sub> to  $\beta$ -Bi<sub>2</sub>O<sub>3</sub> using the ceramic microwave-assisted approach and its increase of capacitance. *Superf. y Vacío* **2019**, *32*, 14–21. [[CrossRef](#)]
2. Leontie, L.; Caraman, M.; Alexe, M.; Harnagea, C. Structural and optical characteristics of bismuth oxide thin films. *Surf. Sci.* **2002**, *507*, 480–485. [[CrossRef](#)]
3. Liu, X.; Xiao, M.; Xu, L.; Miao, Y.; Ouyang, R. Characteristics, Applications and Determination of Bismuth. *J. Nanosci. Nanotechnol.* **2016**, *16*, 6679–6689. [[CrossRef](#)]
4. Gao, X.; Zhang, X.; Wang, Y.; Wang, Y.; Peng, S.; Fan, C. An in vitro study on the cytotoxicity of bismuth oxychloride nanosheets in human HaCaT keratinocytes. *Food Chem. Toxicol.* **2015**, *80*, 52–61. [[CrossRef](#)]
5. Zhao, H.; Tian, F.; Wang, R.; Chen, R. A review on bismuth-related nanomaterials for photocatalysis. *Rev. Adv. Sci. Eng.* **2014**, *3*, 3–27. [[CrossRef](#)]
6. Gadhi, T.A.; Hernández-Gordillo, A.; Bizarro, M.; Jagdale, P.; Tagliaferro, A.; Rodil, S.E. Efficient  $\alpha/\beta$ -Bi<sub>2</sub>O<sub>3</sub> composite for the sequential photodegradation of two-dyes mixture. *Ceram. Int.* **2016**, *42*, 13065–13073. [[CrossRef](#)]
7. Li, X.; Zhu, C.; Song, Y.; Du, D.; Lin, Y. Solvent co-mediated synthesis of ultrathin BiOCl nanosheets with highly efficient visible-light photocatalytic activity. *RSC Adv.* **2017**, *7*, 10235–10241. [[CrossRef](#)]
8. Lin, G.; Tan, D.; Luo, F.; Chen, D.; Zhao, Q.; Qiu, J.; Xu, Z. Fabrication and photocatalytic property of  $\alpha$ -Bi<sub>2</sub>O<sub>3</sub> nanoparticles by femtosecond laser ablation in liquid. *J. Alloys Compd.* **2010**, *507*, L43–L46. [[CrossRef](#)]
9. Tahmasebi, N.; Maleki, Z.; Farahnak, P. Enhanced photocatalytic activities of Bi<sub>2</sub>WO<sub>6</sub>/BiOCl composite synthesized by one-step hydrothermal method with the assistance of HCl. *Mater. Sci. Semicond. Process.* **2019**, *89*, 32–40. [[CrossRef](#)]



10. Zhou, S.X.; Ke, Y.; Li, J.; Lu, S. The first mesostructured bismuth oxychloride synthesized under hydrothermal condition. *Mater. Lett.* **2003**, *57*, 2053–2055. [[CrossRef](#)]
11. Yang, G.W. Laser ablation in liquids: Applications in the synthesis of nanocrystals. *Prog. Mater. Sci.* **2007**, *52*, 648–698. [[CrossRef](#)]
12. Kaur, G.; Kumar, B.; Rai, S.B. Spectroscopic investigations on polyvinyl alcohol film with complex of terbium ions along with bismuth nanoparticles for improved green emission. In *Acrylic Polymers in Healthcare*; IntechOpen: London, UK, 2017.
13. Tian, Z.; Wu, S.; Wang, P.; Cai, Y.; Liang, D.; Ye, Y.; Liang, C. Aqueous dispersed ablated bismuth species and their potential as colloidal Bi precursors in synthetic strategies. *CrystEngComm* **2015**, *17*, 3015–3022. [[CrossRef](#)]
14. Wei, Y.; Zhou, H.; Zhang, H.; Zhu, X.; Liu, G.; Li, Y.; Cai, W. One-Step and Surfactant-Free Fabrication of Gold-Nanoparticle-Decorated Bismuth Oxychloride Nanosheets Based on Laser Ablation in Solution and Their Enhanced Visible-Light Plasmonic Photocatalysis. *ChemPhysChem* **2017**, *18*, 1146–1154. [[CrossRef](#)]
15. Bae, C.H.; Nam, S.H.; Park, S.M. Formation of silver nanoparticles by laser ablation of a silver target in NaCl solution. *Appl. Surf. Sci.* **2002**, *197*, 628–634. [[CrossRef](#)]
16. Sharif, M.; Dorranean, D. Effect of NaCl concentration on silver nanoparticles produced by 1064 nm laser ablation in NaCl solution. *Mol. Cryst. Liq. Cryst.* **2015**, *606*, 36–46. [[CrossRef](#)]
17. Bulmahn, J.C.; Tikhonowski, G.; Popov, A.A.; Kuzmin, A.; Klimentov, S.M.; Kabashin, A.V.; Prasad, P.N. Laser-Ablative Synthesis of Stable Aqueous Solutions of Elemental Bismuth Nanoparticles for Multimodal Theranostic. *Nanomaterials* **2020**, *10*, 1463. [[CrossRef](#)]
18. Zhang, L.; Hashimoto, Y.; Taishi, T.; Nakamura, I.; Ni, Q.Q. Fabrication of flower-shaped Bi<sub>2</sub>O<sub>3</sub> superstructure by a facile template-free process. *Appl. Surf. Sci.* **2011**, *257*, 6577–6582. [[CrossRef](#)]
19. Zhu, M.; Liu, Q.; Chen, W.; Yin, Y.; Ge, L.; Li, H.; Wang, K. Boosting the visible-light photoactivity of BiOCl/BiVO<sub>4</sub>/N-GQD ternary heterojunctions based on internal Z-scheme charge transfer of N-GQDs: Simultaneous band gap narrowing and carrier lifetime prolonging. *ACS Appl. Mater. Interfaces* **2017**, *9*, 38832–38841. [[CrossRef](#)] [[PubMed](#)]
20. Kang, S.; Pawar, R.C.; Pyo, Y.; Khare, V.; Lee, C.S. Size-controlled BiOCl-RGO composites having enhanced photodegradative properties. *J. Exp. Nanosci.* **2016**, *11*, 259–275. [[CrossRef](#)]
21. Jensen, D.S.; Kanyal, S.S.; Madaan, N.; Vail, M.A.; Dadson, A.E.; Engelhard, M.H.; Linford, M.R. Silicon (100)/SiO<sub>2</sub> by XPS. *Surf. Sci. Spectra* **2013**, *20*, 36–42. [[CrossRef](#)]
22. Armelao, L.; Bottaro, G.; Maccato, C.; Tondello, E. Bismuth oxychloride nanoflakes: Interplay between composition-structure and optical properties. *Dalton Trans.* **2012**, *41*, 5480–5485. [[CrossRef](#)] [[PubMed](#)]
23. Narang, S.N.; Patel, N.D.; Kartha, V.B. Infrared and Raman spectral studies and normal modes of  $\alpha$ -Bi<sub>2</sub>O<sub>3</sub>. *J. Mol. Struct.* **1994**, *327*, 221–235. [[CrossRef](#)]
24. Tian, Y.; Guo, C.F.; Guo, Y.; Wang, Q.; Liu, Q. BiOCl nanowire with hierarchical structure and its Raman features. *Appl. Surf. Sci.* **2012**, *258*, 1949–1954. [[CrossRef](#)]
25. Zou, P.; Li, Z.; Jia, P.; Luo, G.; Wang, C. Enhanced photocatalytic activity of bismuth oxychloride by in-situ introducing oxygen vacancy. *Colloids Surf. A Physicochem. Eng. Asp.* **2021**, *623*, 126705. [[CrossRef](#)]
26. Motakef-Kazemi, N.; Yaqoubi, M. Green synthesis and characterization of bismuth oxide nanoparticle using mentha pulegium extract. *Iran. J. Pharm. Res. IJPR* **2020**, *19*, 70.
27. Li, L.; Zhang, M.; Zhao, Z.; Sun, B.; Zhang, X. Visible/near-IR-light-driven TNFePc/BiOCl organic-inorganic heterostructures with enhanced photocatalytic activity. *Dalton Trans.* **2016**, *45*, 9497–9505. [[CrossRef](#)]

**Disclaimer/Publisher's Note:** The statements, opinions and data contained in all publications are solely those of the individual author(s) and contributor(s) and not of MDPI and/or the editor(s). MDPI and/or the editor(s) disclaim responsibility for any injury to people or property resulting from any ideas, methods, instructions or products referred to in the content.